



A direct *in situ* observation of water-enhanced proton conductivity of Eu-doped ZrO₂: Effect on WGS reaction

Nuria García-Moncada*, Luis F. Bobadilla, Rosalía Poyato, Carlos López-Cartes, Francisca Romero-Sarria, Miguel Ángel Centeno, José Antonio Odriozola

Instituto de Ciencia de Materiales de Sevilla and Departamento de Química Inorgánica, Centro Mixto CSIC-Universidad de Sevilla, Av. Américo Vespucio 49, 41092, Sevilla, Spain

ARTICLE INFO

Keywords:

Eu-doped zirconia
Solid solution
Proton conductivity
WGS reaction

ABSTRACT

Eu-doped ZrO₂ solid solutions have been synthesized in order to prepare proton conductors as water-enhancer additives for the WGS reaction. Elemental characterization has been carried out revealing homogeneous dopant distribution resulting in fluorite-type solid solutions for Eu₂O₃ contents up to ~9 mol.%. Representative samples of the Eu-doped ZrO₂ series have been analysed by Impedance Spectroscopy (IS) in inert, oxygen and wet conditions. The solid solution with 5 mol.% of Eu₂O₃ has presented the highest conductivity values for all tested conditions indicating an optimal amount of dopant. Moreover, the presence of vapour pressure results in an increment of the conductivity at temperatures lower than 300 °C, meanwhile at higher temperatures the conductivity is the same than that in inert conditions. To elucidate these results, *in situ* DRIFTS studies were carried out. These experiments evidenced the existence of water dissociation at oxygen vacancies (band at 3724 cm⁻¹) as well as the presence of physisorbed water at temperatures up to ~300 °C where the band at 5248 cm⁻¹ characteristic of these species disappeared. These results points to a layer model where the physisorbed water interacts with surface hydroxyls generated by dissociated water that improves the proton conductivity through Grotthuss' mechanism in the RT-300 °C temperature range. These samples were successfully tested in WGS reaction as additive to a typical Pt-based catalyst. The presence of the mixed oxide reveals an increase of the catalyst' activity assisted by the proton conductor, since improves the water activation step.

1. Introduction

Ionic conductors and, more specifically, proton conductors are very attractive for a wide range of technological applications, e.g. mixed ionic-electronic conducting (MIEC) oxides as gas sensors, as catalysts, for clean energy production, for oxygen/hydrogen separation membranes [1,2], or in solid-oxide fuel cells (SOFCs) to convert the chemical energy of fuels into electrical energy [3].

Generally, high temperature ion conductors consist in oxide materials doped with aliovalent cations. For instance, this is the case of acceptor-doped perovskites (ABO₃) where the substitution of A-site or B-site cations for others metals with different oxidation state creates oxygen vacancies [4,5]. The conduction mechanism depends on the oxide structure, the carrier species and the created defects (electronic or structural) [6,7]. Different conduction mechanisms have been proposed such as the hopping mechanism or the Grotthuss' mechanism [8,9]. Regardless the conduction mechanism, the high stability of these structures and the presence of oxygen vacancies allow the conductivity

of ions like O²⁻, OH⁻ or H⁺. However, synthesis of materials with both high ionic conductivity and high stability has been challenging during the last years [10]. For example, BaCeO₃-based perovskites was reported to present high conductivity but they showed very low phase stability, whereas CaZrO₃ materials exhibits good stability but very low conductivity [11]. In this context, cubic zirconium based oxides have been extensively studied owing to the good stability of doped zirconia, easily synthesized to obtain cubic structures (perovskite, pyrochlore or fluorite-type structures) [12,13]. Thus, doping zirconia with aliovalent cations creates good ionic conductors with high stability. Magrasó et al. [14] reported ionic conductivities for BaZrO₃ in wet atmospheres at 700 °C in the range of 10⁻⁴ S cm⁻¹, and Babilo et al. [15] found a conductivity of 7.9 · 10⁻³ S cm⁻¹ for BaZr_{0.8}Y_{0.2}O_{3-δ} at 600 °C under humidified nitrogen in an attempt to prepare BaZrO₃ based compounds with reproducible conductivities. These are state-of-art electrolyte materials for proton conductivity showing high proton conductivity within the material grains (~10⁻² S cm⁻¹) with good chemical and mechanical stability but high resistance at grain boundaries.

* Corresponding author.

E-mail address: nuria.garcia@icmse.csic.es (N. García-Moncada).

Besides perovskite-type materials, the conductivity and stability of pyrochlore/fluorite type oxides has also been studied [16,17]. In general, doping with rare earth metals (La, Sm, Eu, Gd...) results in enhanced chemical stability and good ionic conductivity at temperatures lower than undoped oxides. In this context, conductivities of $\sim 10^{-2} \text{ S cm}^{-1}$ at 900°C and $\sim 10^{-3} \text{ S cm}^{-1}$ at 600°C were reported by Xia et al. [18] for Sm- and Eu-doped zirconium oxide.

Water plays a crucial role in many catalytic processes. Water may interact with oxide surfaces forming weak bonds (physisorbed layers) or forming strong bonds through dissociative chemisorption resulting in hydroxyl saturated surfaces. Three main processes involving water in catalytic processes may be considered: (i) a promotional role of molecular water including the solvation-like effect and water-mediated H-transfer, (ii) a promotional role of OH/OH^- and H/H^+ species, and (iii) miscellaneous effects of water, such as water-assisted carbon removal, surface reconstruction, and active sites blocking [19]. Concretely, the rate limiting step in the water gas shift (WGS) reaction involves the activation of water species on the catalyst surface that may occur either at the active metal sites or at the support surface [20–25]. The adsorption and activation of water molecules is being a subject of intensive interest in order to clarify the role of metals and supports and the catalytic activity of the WGS catalysts. A DFT study of water dissociation on Pt(111) results in supporting the formation of hydroxyl groups on the Pt surface under H_2 -rich atmospheres [23]. The activation energy for adsorbed water dissociation into adsorbed OH and H species on Pt(111) is estimated to be 72 kJ mol^{-1} in close agreement with the results of Michaelides et al. [26] and Grabow et al. [27] that reported 66 and 85 kJ mol^{-1} , respectively. Experimentally, activation energies in the range $68\text{--}86 \text{ kJ mol}^{-1}$ have been calculated for Pt/ Al_2O_3 , Pt/ CeO_2 and Pt/ $\text{CeO}_2\text{-Al}_2\text{O}_3$ catalysts [20,21,24,28–32]. These values are also close to those found both experimental (61 kJ mol^{-1}) and theoretically (67 kJ mol^{-1}) for Pt/ TiO_2 catalysts [33]. The interaction of H_2O with the CeO_2 surface has been the object of numerous studies since its implication in many catalytic reactions. As reviewed by Mullins [34], molecular and dissociated water molecules are evidenced on the ceria surface although several explanations are given on their relative stability. DFT and molecular dynamics simulations of water adsorption/activation on oxidized and reduced CeO_2 (111) surfaces have shown that the heterolytic dissociation of H_2O is the most favourable path occurring with a very low activation barrier of less than 10 kJ mol^{-1} [35]. Guild et al. [36] reported and experimental and theoretical study of the WGS on CeO_2 (100) surfaces. These authors also propose the heterolytic water dissociation on ceria as the most probable path on both oxidized and reduced (100) ceria surface. Further studies on the interaction of H_2O with the (100) surface of ceria nanocubes using MAS ^1H NMR have also shown an almost barrier free water dissociation [37]. However, DFT studies on model Pt/ CeO_2 (111) catalysts by Lykhach et al. [38] suggest that adsorption of molecular water on stoichiometric ceria terraces is favoured over dissociatively adsorbed water but dissociation is favoured on partially reduced CeO_2 (111) surfaces. The enhancement of water dissociation on partially reduced ceria has also been evidenced experimentally [39–43]. On the other hand, Aranifard et al. [44] have shown that for Pt/ CeO_2 catalysts H_2O dissociation at the metal support interface only occurs after attaining a complete surface coverage by hydroxyl groups of the ceria surface. Therefore, the hydroxyl coverage of the support is a key parameter in the catalytic activity in the WGS reaction.

In previous studies we have shown that the support ability to promote surface water diffusion determines the catalytic activity [24]. To boost the catalytic activity of conventional Pt-based catalysts for the WGS reaction its mechanical mixing with ionic conductors has been proposed by us; this substantially improves the catalyst performances [45]. Therefore, to comprehend the key role played by water in this reaction, it is essential a mechanistic understanding of the promotional effect caused by the ionic conductor. The knowledge of the adsorption and activation of water molecules on the catalyst surface is thereby

imperative to develop more efficient catalysts.

In the present work, we analyse the ionic conductivity and the structure of a rare-earth (europium) doped zirconium oxide using a combination of *in situ* Diffuse Reflectance Fourier Transform Infrared Spectroscopy (DRIFTS), Raman spectroscopy, and impedance spectroscopy (IS) under different conditions of moisture and temperature. Furthermore, we have studied the influence of the physical mixture of the ionic conductor with a typical Pt-based catalyst in the performance of the WGS reaction. In this respect, the main objective is to correlate the surface changes caused by the adsorption of water with the ionic conductivity of the materials and their water-promotional effect in the WGS reaction.

2. Experimental procedure

2.1. Preparation of materials

Europium-doped ZrO_2 materials with different amounts of Eu_2O_3 (2, 5, 7, 9, 10, 12 and 15 mol.% of Eu_2O_3 , named as ZrEu_x , where x is the mol.% of the Eu_2O_3) were prepared by co-precipitation. An appropriate amount of 0.1M aqueous solution of europium (III) nitrate pentahydrate (Sigma-Aldrich) was slowly added to a 0.1 M aqueous solution of zirconium (IV) oxynitrate hydrate (Sigma-Aldrich) under continuous stirring. The initial pH value of the solution was in the 1–2 range, then the pH was increased until 8 by adding an ammonia solution (30 vol.%, Panreac). Afterwards, the solution was aged for 1.5 h at room temperature under stirring. The obtained white precipitate was filtered and washed with distilled water and then submitted to dryness at 100°C overnight. Finally, the solid was calcined in air at 500°C for 5 h to remove the nitrate leftovers.

The Pt-based catalyst (labelled PtCeAl) for the catalytic tests in WGS reaction was used following a preparation method previously reported by our research group [24]. A 2 wt.% of Pt was loaded over a commercial $\text{CeO}_2/\text{Al}_2\text{O}_3$ (mass ratio of 20:80 of ceria/alumina, Puralox) by wet impregnation method. The final catalyst was calcined at 350°C for 8 h.

2.2. Elemental characterization

The chemical composition of the prepared solids was obtained by X-ray fluorescence spectrometry (XRF) using an AXIOS PANalytical spectrometer with Rh source of radiation.

The textural properties of the materials were determined by N_2 adsorption at liquid nitrogen temperature using a Micromeritics Tristar II instrument. Previously, the samples were degassed at 250°C for 4 h in vacuum.

The XRD structural analysis of the solids was performed on an X'Pert Pro PANalytical instrument. Diffraction patterns were obtained using $\text{Cu K}\alpha$ radiation (40 mA, 45 kV) over a 2θ -range of $10\text{--}90^\circ$ and using a step size of 0.05° and a step time of 80 s.

X-ray photoelectron spectra (XPS) from calcined powders were recorded on a Leybold-Heraeus LHS-10/20 spectrometer equipped with an ultra-high vacuum (UHV) system operating at $5 \cdot 10^{-9}$ Torr and a dual X-ray source, of which the $\text{Al K}\alpha$ (1485 eV) was used. Binding energy correction was performed by fixing C 1s level at 284.6 eV. Spectra were analysed with CasaXPS software and Gaussian-Lorentzian (70:30) curves were used for the fittings. Narrow scans were acquired at binding energy intervals associated with the Zr 3d, Eu 3d, O 1s and C 1s levels. In order to quantify the band areas and obtain superficial atomic percentages, Zr 3d_{5/2} and Eu 3d_{5/2} peaks areas corrected with their respective Scofield factors for Al K α source were used.

Transmission Electron Microscopy (TEM) micrographs were recorded on a Philips CM-200 instrument. Powder samples were supported on a holey carbon-coated copper grid without using any liquid.

The UV-vis spectra were recorded on an Avantes spectrometer model AvaLight-DH-S-BAL. All the spectra were collected in absorbance

mode using BaSO₄ as reference.

Raman spectroscopy analysis was carried out in a dispersive Horiba Jobin Yvon LabRam HR800 microscope. Raman spectra were obtained by using a 532.14 nm laser excitation source with a $\times 50$ microscope objective. The power of the laser on the sample is 20 mW with a 600 g mm⁻¹ grating. Two types of filters were used: D1 filter which reduces the laser to 2 mW to avoid a saturated signal in the 1000–4000 cm⁻¹ range, and D0.6 filter to have a laser of 5 mW for the 200–1000 cm⁻¹ range. A confocal pinhole of 1000 μ m was employed for all the measurements reported. Prior to the analysis, the Raman spectrometer was calibrated using a silicon wafer reference.

2.3. Ionic conductivity measurements

In order to analyse the conductivity, calcined powders were sintered by Spark Plasma Sintering (SPS) technique in a Dr. Sinter Inc. Instrument (Kanagawa, Japan) model 515S equipped with a 10 mm diameter cylindrical graphite die/punch setup in a vacuum chamber. The sintering temperature was 900 °C for 5 min with a heating rate of 100 °C min⁻¹ and the applied uniaxial pressure was 50 MPa. Pellets were then cooled to room temperature and polished in order to eliminate the carbon deposited on the surface. This treatment does not modify phase composition as stated by XRD. The conductivity measurements were performed in an impedance spectrometer Agilent (HP) model 4294A over a frequency range of 100 Hz to 4 MHz with an AC voltage of 0.1 V. Pellets were previously coated with silver by painting both surfaces of the pellets with a colloidal solution and then removing the solvent at 600 °C in Ar for 3 h. The silver coating is the contact film between sample and platinum electrodes. The impedance measurements were carried out from room temperature to 700 °C in a flow of Ar, O₂/Ar (from 10 to 100% of oxygen) and H₂O/Ar (20 vol.% of water), thereby studying the influence of oxygen and water on the conductivity. Before the impedance measurements, the samples were dehydrated *in situ* in dry air at 600 °C for 3 h.

2.4. In situ spectroscopic experiments

In situ Raman experiments were performed in a Linkam CCR1000 cell coupled to the Raman spectrometer equipment. This cell is capable of operating under flow conditions up to 1000 °C. The sample was initially dehydrated *in situ* at 450 °C for 1 h with a heating rate of 10 °C min⁻¹ in a flow of 50 mL min⁻¹ of nitrogen. Afterwards, the sample was cooled down to 200 °C and a flow of 50 mL min⁻¹ of nitrogen saturated with water at room temperature was introduced. The temperature was increased up to 450 °C recording a spectrum every 50 °C after 15 min stabilization using the same experimental conditions mentioned above.

In situ DRIFTS measurements were performed in order to investigate the effect of adsorption/dissociation of water on the samples and establish an ionic conductivity–structure correlation. The experiments were carried out in a THERMO/Nicolet model iS50 spectrometer equipped with a MCT detector and a Praying Mantis High Temperature Reaction chamber with ZnSe windows (Harrick). Spectra were obtained by averaging 32 scans with a resolution of 4 cm⁻¹. Typically, 200 mg of sample was placed in the Harrick reaction chamber. The spectrometer bench was continuously purged with pure nitrogen to eliminate CO₂ and water vapour contributions to the spectra. The background spectrum was collected without sample using an aluminium mirror. Before water adsorption, the samples were dehydrated *in situ* at 600 °C for 1 h in 50 mL min⁻¹ of a 10% H₂/Ar flow and then cooled down to 200 °C under Ar flow. Finally, the study of water adsorption was performed passing through the sample a flow of 50 mL min⁻¹ of 10% H₂O/Ar and increasing the temperature from 200 to 450 °C. For it, the adequate amount of water was fed continuously by using a HPLC pump and vaporising the liquid in a homemade evaporator.

2.5. Catalytic activity in WGS reaction

The WGS reaction has been carried out at atmospheric pressure in a home-made rig coupled to an on-line ABB gas analyser (AO2020) equipped with an IR detector in a tubular fixed bed reactor of 9 mm in diameter. The catalytic tests were studied in the temperature range of 180 °C to 350 °C using a feed of 4.5% of CO, 30% of H₂O and N₂ as balance. Previously, the catalysts were reduced in 10% of H₂ balanced with N₂ for 30 min at 350 °C. The space velocity was 80,000 mL h⁻¹ g_{cat}⁻¹ respect to the 0.1 g of PtCeAl catalyst used in all the experiments. Physical mixtures of PtCeAl and an ionic conductor in a mass ratio of 1:5 (to ensure a complete contact with the ionic conductor) as well as PtCeAl alone were studied. Particles sizes sieved between 600 and 800 μ m were selected and the catalytic bed volume was always of 0.4 cm³ (adding inert quartz in the same particle size when is needed), providing an also constant volumetric space velocity of 20,000 h⁻¹.

3. Results and discussion

3.1. Crystal structure, physicochemical properties and morphology

The cation radius of the Eu³⁺ dopant, 0.95 Å, is slightly higher than that of the Zr⁴⁺ cation, 0.84 Å, of the hosting lattice. Despite the good matching between the cation radii ZrO₂ and Eu₂O₃ are not completely miscible and, therefore, cubic solid solutions appear just in a limited compositional range. These solid solutions may contain a relative large number of environments for Eu³⁺ cations, from isolated ions to large associates of Eu³⁺ ions with oxygen vacancies [46]. For Eu:Zr molar concentrations 1:1 oxygen vacancies order and cubic pyrochlore structures develop [47]. The lattice constant of low Eu content defective fluorite solid solutions follows Vegard's law, which implies an enlargement of the lattice constant as well as an increase in the number of oxygen vacancies [47]. Deviations from this model may be due to the existence of short-range pyrochlore-like structures over the extended defect fluorite structure of the solid solution [48]. To elucidate the structural properties of the prepared materials XRD measurements were carried out. In Fig. 1a it is shown the diffractograms of the prepared samples once calcined. For Eu₂O₃ loadings below 9 mol.%, the solids maintain a cubic fluorite type structure (Fm $\bar{3}$ m) characteristic of Eu-doped ZrO₂ solid solution [47–49]. All the diffraction peaks slightly shift toward lower angles on adding europium to the ZrO₂ phase. At higher europium loadings, either a segregated europium oxide phase or short-range defect ordering appears. A close inspection of the diffraction line corresponding to the (111) crystallographic plane, Fig. 1b, allows noticing the enlargement of the FWHM on increasing the Eu content as well as the presence of a shoulder that may be compatible with both the presence of a segregated europium oxide phase and of short-range defect ordering producing pyrochlore-like structures within the cubic material. At the highest Eu₂O₃ contents analysed diffraction lines tend to overlap, which difficult further analysis. Therefore, 9 mol.% Eu₂O₃ corresponds to the maximal content of europium allowed in the host zirconium lattice. In consequence with this experimental observation, we can establish that the limit of solubility of Eu₂O₃ in ZrO₂ resulting in homogeneous defect fluorite solid solutions is around 9 mol.% of Eu₂O₃. Fig. 1c shows the relationship between the estimated lattice parameters and the europium content reflecting all the above considerations.

Table 1 includes the crystallite sizes estimated by using the Scherrer's Equation on the (111) crystallographic plane of the solid solution. Overall, it should be noted a decrease of the crystallite size when increasing the europium content, this behaviour is similar to that previously observed for the solid solutions formed between CeO₂ and aliovalent trivalent cations including europium [50,51]. The crystallite size trend is usually associated with surface energetics and is related to the number of surface oxygen vacancies induced by doping with

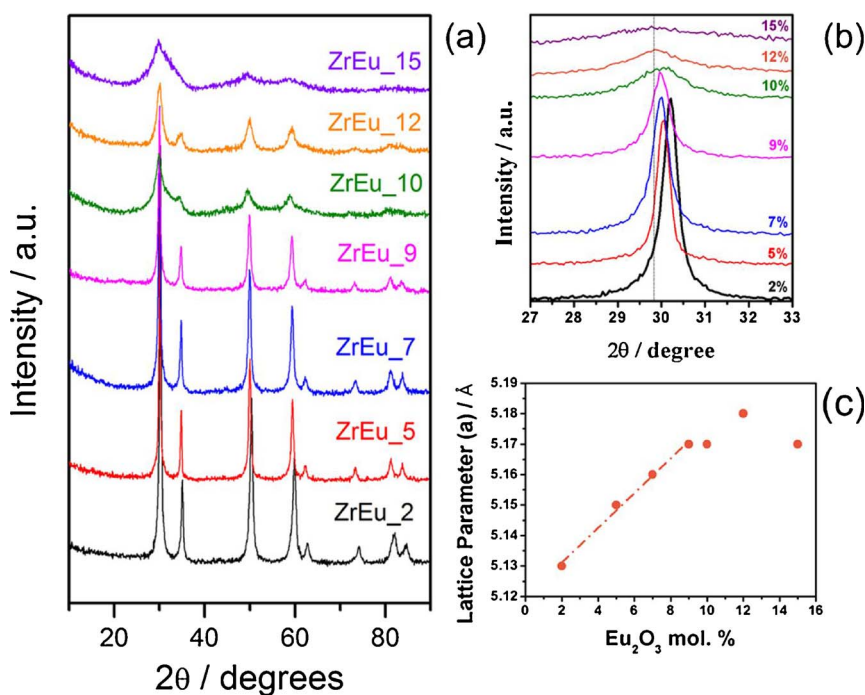


Fig. 1. XRD of the synthesized samples: a) complete diffractograms, b) magnified zone on the (111) crystallographic plane and c) calculated lattice parameters of the samples.

Table 1
Chemical composition, crystallite sizes and textural properties of calcined samples.

Sample code	Chemical composition (Eu ₂ O ₃ mol.%) ^a	Crystallite size (nm)	S _{BET} (m ² g ⁻¹)	Pore volume (cm ³ g ⁻¹)	Pore size (nm)
ZrEu ₂	2.35 (2)	24	68	0.072	3.8
ZrEu ₅	6.04 (5)	33	42	0.020	3.4
ZrEu ₇	9.10 (7)	21	19	0.015	2.2
ZrEu ₉	–	19	25	0.021	2.4
ZrEu ₁₀	–	6	10	0.008	2.3
ZrEu ₁₂	13.51 (12)	–	9	0.007	2.5
ZrEu ₁₅	–	–	1	0.001	3.1

^a Eu₂O₃ mol.% determined by XRF. Among parentheses are presented the nominal values of Eu₂O₃.

aliovalent cations in ZrO₂ or CeO₂ matrices [52]. This crystal growth pinning induced by the presence of dopants may be overestimated due to the presence of other phases, as stated above, that may appear on increasing the Eu content.

The textural properties of the prepared samples once calcined are summarized in Table 1. The specific BET surface area, pore volume and average pore radius decreases on increasing the europium content. A monomodal pore size distribution (not shown) with diameters in the range 2–4 nm is always observed.

On the basis of the textural properties and XRD data, samples containing 2, 5, 7 and 12 mol.% of Eu₂O₃ were selected as representative materials and, therefore, submitted to more specific characterizations. ZrEu₂ and ZrEu₅ are the samples with the highest BET surface area and ZrEu₁₂ sample consist in a solid solution containing Eu up to the solubility limit together with segregated europium oxide phase. The chemical composition measured by XRF is in fairly good agreement with the target values, Table 1. On analyzing the bulk-to-surface atomic ratios of Eu and Zr by XPS (Fig. 2) it is clear that for all solid solutions are quite homogeneous being the surface and bulk compositions almost identical. On the other hand, it is evident that in the ZrEu₁₂ sample an excess of Eu oxide remains on the surface likely forming a segregated europium oxide phase in good agreement with the results obtained by XRD.

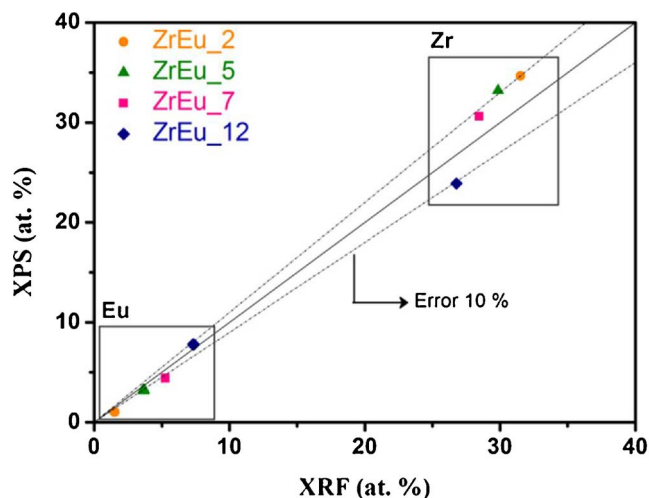


Fig. 2. Comparison of the atomic percent of Eu and Zr determined by XPS in the surface and XRF in the bulk for the samples ZrEu_x (x = 2, 5, 7 and 12). Representation of the deviation of 10% (dot line) from the ideal homogeneous solid solution (solid line).

The monomodal porous size distribution is confirmed by TEM. Fig. 3 presents the TEM analysis for the samples ZrEu₂, ZrEu₅, ZrEu₇ and ZrEu₁₂ showing in all cases a high porosity of the samples. Moreover, the average pore diameters measured using TEM images for every sample (between 2 and 3 nm) are consistent with the values obtained by N₂ adsorption. On the other hand, it is also noticeable that the pore concentration decreases on increasing the europium content. This suggests the formation of a segregated europia phase as above mentioned.

All the synthesized Eu-doped zirconia compounds exhibit a polycrystalline nature. For example, the inspection of the images of the ZrEu samples shown in Fig. 3 could lead us to confirm the presence of particles constituted by very small oxide crystals. However, in some cases the analysis, by selected area electron diffraction (SAED), of this type of particles clearly demonstrates their monocrystalline character. The electron diffraction pattern shown as an inset in Fig. 3 corresponds to

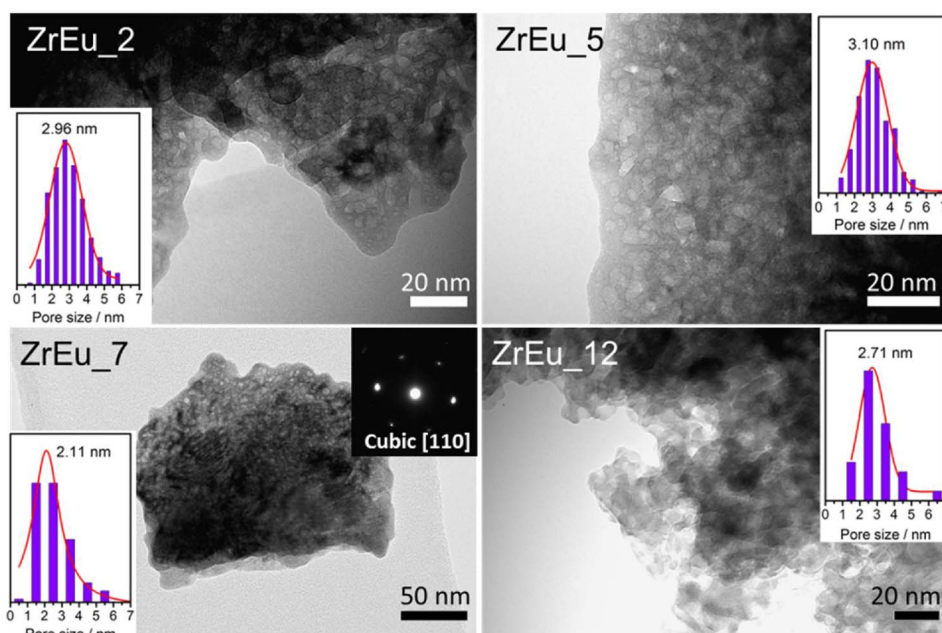


Fig. 3. TEM micrographs and pore size distribution of the samples ZrEu_x (x = 2, 5, 7, 12).

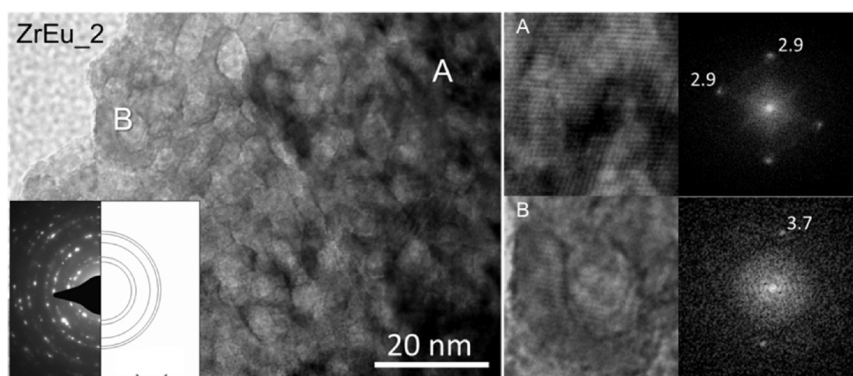


Fig. 4. TEM micrograph and electron diffraction diagrams of the selected areas of the sample ZrEu₂.

the ZrEu₇ particle of the figure. A typical electron diffraction pattern taken along [111] zone axis of the cubic phase is clearly recognized. In Fig. 4, a different electron diffraction pattern taken from a larger area on sample ZrEu₂ is shown. The presence of typical diffraction rings demonstrates the polycrystalline nature of the sample. The observed rings are mainly due to the presence of the fluorite structure of the mixed oxide as revealed by their match with the first five theoretical reflections, inset in the image. Apart of these characteristic rings, some other reflections, in the form of light weak spots between the second and third rings, are observed on the experimental diffraction pattern. The measurements of the d-spacing that originates these extra spots are in agreement with the (211) planes of a zirconium oxide monoclinic phase. Focusing on the analysis of High Resolution Images, it is also possible to distinguish different nanocrystals showing both cubic and monoclinic structure. In this sense, zone A of image in Fig. 4 shows periodic contrasts at 2.9 Å which can be assigned to (111) planes of the cubic structure. The digital diffraction pattern (DDP) obtained from this image corresponds to the [110] zone axis of the fluorite structure of the mixed oxide. On the contrary, the monoclinic phase is detected in the zone B of the image. The interplanar spacing of 3.7 Å could be associated to the (001) or (110) planes of the monoclinic phase. Other areas have been analysed and interplanar spacings of 5.0 Å, according to the (100) planes of the monoclinic phase, have been measured. These observations are in agreement with the presence of the monoclinic phase

in the ZrEu₂ sample, indicating that in some parts of the solid exist segregated monoclinic ZrO₂ due to the poor europium content in this sample. For samples containing above 5 mol.% of Eu₂O₃, the cubic structure is identified as the unique phase according to the formation of the solid solution analysed by XRD.

In light of the exposed results, we can deduce that the used synthesis method results in homogeneous solid solutions, in which a homogeneous oxygen vacancies distribution is expected.

3.2. UV-vis and Raman spectroscopy

Fig. 5 displays the UV-vis absorption spectra of the ZrEu₅, ZrEu₇ and ZrEu₁₂ samples as well as that of a monoclinic ZrO₂ reference sample for comparison. As shown in Fig. 5, the presence of Eu³⁺ ions in the host zirconia structure provokes the appearance of a strong charge transfer transition band below 350 nm that exhibits a red-shift on increasing the europium content. This phenomenon can be explained by a narrowing of the band gap, by the appearance of intragap energy levels caused by the dopants or by the absorption caused by the created oxygen vacancies as reported by Serpone [53]. Besides this strong absorption feature in the UV region, much weaker characteristic absorptions ascribed to Eu³⁺ were also identified. These can be assigned to transitions from the ⁷F₀ ground state to ⁵D₁, ⁵D₂ and ⁵L₆ states of Eu³⁺, respectively [54–56].

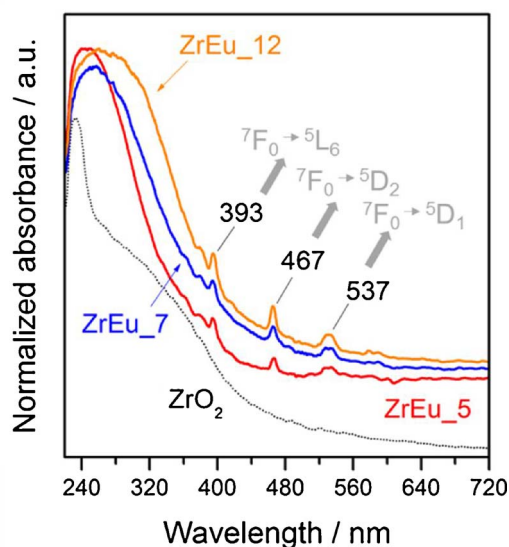


Fig. 5. UV-vis spectroscopy at room temperature of the synthesized samples and ZrO_2 spectrum as a reference for comparison.

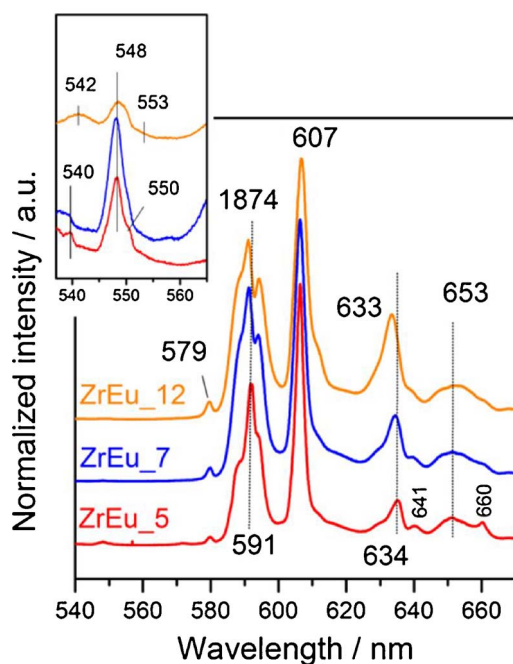


Fig. 6. Luminescence spectra extracted from *ex situ* Raman spectroscopy of the synthesized samples at room temperature.

Fig. 6 shows the Raman spectra of the ZrEu_5, ZrEu_7 and ZrEu_12 samples where $f \rightarrow f$ electronic transitions due to the europium luminescence caused by the excitation at 530 nm dominate. In fact, the zirconia Raman spectrum is hidden by the europium luminescence. Table 2 compiles all the transitions according to the Raman shift position and the total absorption energy [57,58]. The luminescence profiles (wavelengths, relative intensities and widths) of these samples are in general similar to those observed for Eu^{3+} ions in other materials [59–61]. In general, transitions towards the $^5\text{D}_1$ excited state are observed at wavenumbers below 560 nm (Raman shift less than $\sim 1000 \text{ cm}^{-1}$). At 579 nm the $^7\text{F}_0 \rightarrow ^5\text{D}_0$ transition occurs, this transition only appears for Eu^{3+} ions with low symmetries which indicate that Eu ions are associated to oxygen vacancies. The $^7\text{F}_1 \rightarrow ^5\text{D}_0$ transition is identified at $\sim 591 \text{ nm}$. This transition splits in three components between 588 and 594 nm (1791, 1860 and 1954 cm^{-1} Raman shifts),

Table 2

$f \rightarrow f$ transitions for synthesized Eu doped zirconia compounds.

Raman Shift (cm^{-1})	Wavelength (nm)	Transition	Raman Shift (cm^{-1})	Wavelength (nm)	Transition
260	540	$^7\text{F}_2 \rightarrow ^5\text{D}_1$	1954	594	$^7\text{F}_1 \rightarrow ^5\text{D}_0$
		$^7\text{F}_1 \rightarrow ^5\text{D}_1$			
327	542	$^7\text{F}_2 \rightarrow ^5\text{D}_1$	2324	607	$^7\text{F}_2 \rightarrow ^5\text{D}_0$
		$^7\text{F}_1 \rightarrow ^5\text{D}_1$			
560	548	$^7\text{F}_2 \rightarrow ^5\text{D}_1$	2443	612	$^7\text{F}_2 \rightarrow ^5\text{D}_0$
		$^7\text{F}_1 \rightarrow ^5\text{D}_1$			
628	550	$^7\text{F}_2 \rightarrow ^5\text{D}_1$	2985	633	$^7\text{F}_2 \rightarrow ^5\text{D}_0$
		$^7\text{F}_1 \rightarrow ^5\text{D}_1$			
720	553	$^7\text{F}_2 \rightarrow ^5\text{D}_1$	3024	634	$^7\text{F}_2 \rightarrow ^5\text{D}_0$
		$^7\text{F}_1 \rightarrow ^5\text{D}_1$			
1530	579	$^7\text{F}_0 \rightarrow ^5\text{D}_0$	3180	641	$^7\text{F}_3 \rightarrow ^5\text{D}_0$
1791	588	$^7\text{F}_1 \rightarrow ^5\text{D}_0$	3460	652	$^7\text{F}_3 \rightarrow ^5\text{D}_0$
			3472	653	
1860	591	$^7\text{F}_1 \rightarrow ^5\text{D}_0$	3645	660	$^7\text{F}_3 \rightarrow ^5\text{D}_0$

this splitting necessarily indicates that the symmetry is orthorhombic or less which again points to the association between Eu and oxygen vacancies [57]. Therefore, as stated by Goff et al. [62] the oxygen vacancies defect clusters depend on the concentration of the aliovalent cations justified the modification observed in the $^7\text{F}_1 \rightarrow ^5\text{D}_0$ transition upon the increase of the europium concentration. The transition $^7\text{F}_2 \rightarrow ^5\text{D}_0$ (around 607 nm), at higher Raman shifts, is strongly influenced by the local symmetry of Eu^{3+} ion and the nature of the ligands. According to several authors [59–61,63], the relative intensity of the $^7\text{F}_2 \rightarrow ^5\text{D}_0$ transition is higher than that of the $^7\text{F}_1 \rightarrow ^5\text{D}_0$. The intensity ratio ($^7\text{F}_2 \rightarrow ^5\text{D}_0$)/($^7\text{F}_1 \rightarrow ^5\text{D}_0$) relates to the symmetry of the Eu coordination environment; thus, the lower the ratio, the higher the site symmetry. In these samples, the ($^7\text{F}_2 \rightarrow ^5\text{D}_0$)/($^7\text{F}_1 \rightarrow ^5\text{D}_0$) ratio increases with the Eu content, this is, there is a loss of symmetry of the europium site on increasing the Eu content, indicating again the association of the Eu atoms and the oxygen vacancies. Moreover, the $^7\text{F}_2 \rightarrow ^5\text{D}_0$ transition is also affected by the contribution of emissions from higher excited states ($^5\text{D}_1$, $^5\text{D}_2$, $^5\text{D}_3$) in this energy range [57], as it can be noticed in the 634 nm signal that shifts to higher energies on increasing the europium loading and, at the same time, an increase in its intensity is also observed.

3.3. Ionic conductivity measurements

The impedance measurements of the studied Eu-doped zirconia samples were measured as a function of the gaseous environment. Three different atmospheres were analysed, argon, oxygen-argon and wet argon, oxygen and water partial pressures were swept in a wide range to study their influence on the conducting properties of the Eu-doped materials. For every gaseous condition, the impedance experiments were performed from room temperature to 700°C in order to estimate the activation energy (E_a) for the conduction process by Arrhenius equation.

The impedance complex plane plots, in all cases, show distinguishable impedance arcs over 200°C . Complex impedance plots measured at 350°C for all solids in Ar and 20% H_2O in Ar are plotted in Fig. 7a and b, respectively. Two arcs accounting for bulk and grain boundary conduction are clearly shown in Ar dry condition for ZrEu_2, ZrEu_5 and ZrEu_7 samples. The total impedance of these materials is significantly lower ($\sim 10^5 \Omega \text{ m}$) than that of the ZrEu_12 sample ($\sim 10^6 \Omega \text{ m}$). Moreover, the difference between the characteristic frequencies of both conduction processes (bulk and grain boundary, represented in Fig. 7a) decreases on increasing the europium content resulting in just one arc for the sample containing 12 mol.% of dopant. Unlike the capacitance or the resistance, which depend on the geometry, the characteristic frequency only depends on the material

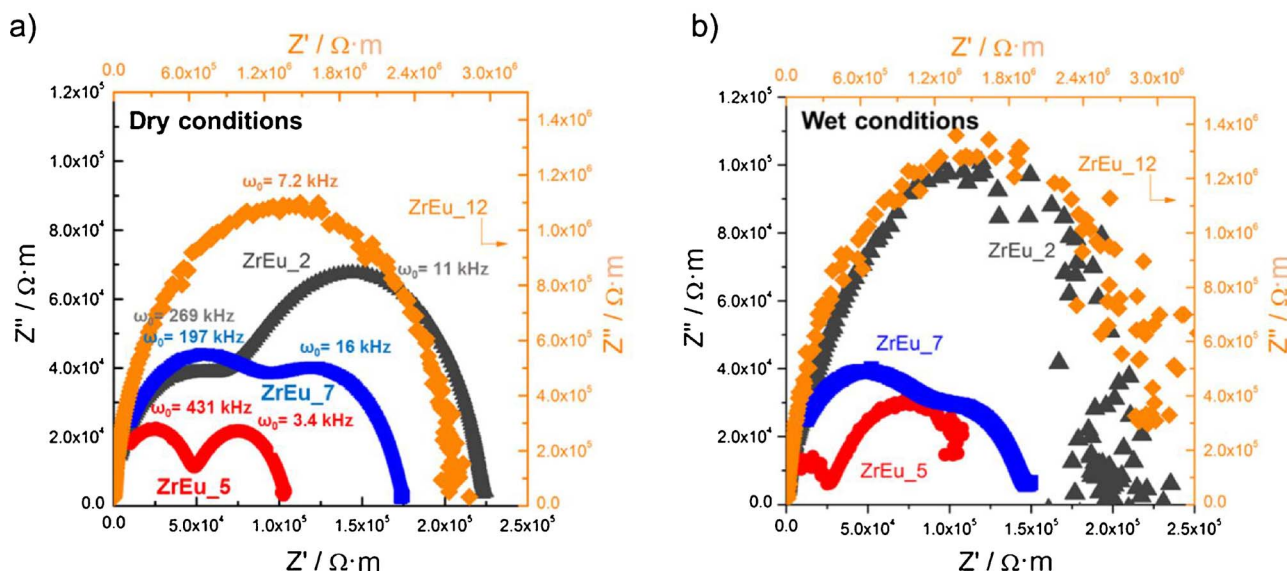


Fig. 7. Complex plane plots of the impedance spectroscopy of the sintered samples at 350 °C in (a) dry conditions (in Ar atmosphere) and (b) wet conditions with 20% H₂O.

nature. This allows to measure bulk, grain boundary and total impedances, as well as their conductivities of ZrEu₂, ZrEu₅ and ZrEu₇ samples. However, as the impedance data for the ZrEu₁₂ solid show only one arc, these data are not enough by themselves to reveal the magnitudes of either bulk or grain boundary conductivities [64].

The highest total conductivity (lowest impedance), in the studied temperature range, is observed for the ZrEu₅ sample as observed in Figs. 7 and 8, for both dry and wet Ar. Therefore, the conductivity reaches a maximum for 5 mol.% of Eu₂O₃. Whatever the temperature, the shapes of the impedance arcs are similar to those observed at 350 °C, Fig. 7, for the four analysed samples, but for a proportional reduction of the impedances on increasing temperature that agrees with a typical semiconductor behaviour for which conductivity increases with temperature. By using these calculated conductivities, the activation energies for the conduction processes were estimated (Fig. 8). The calculated activation energies vary from 0.953 to 1.220 eV on increasing the Eu content of the studied solids, Table 3. These values, according to the literature [65], are characteristic of pure ionic conductors (~1 eV). Acceptor-doped ZrO₂ compounds have been reported

Table 3

Total activation energies (eV) of the ionic conductors in different atmospheres.

Sample	Inert (Ar)	O ₂ /Ar	Wet Ar	
			20% H ₂ O	50% H ₂ O
ZrEu ₂	0.953	0.951	0.982	0.988
ZrEu ₅	1.055	1.067	1.063	1.073
ZrEu ₇	1.062	1.086	0.993	1.098
ZrEu ₁₂	1.220	1.217	1.199	-

* ZrEu₁₂ sample presents an uncertain value of conductivity in presence of water due to its high porosity, since the pores are filled with water and the conductivity measurement is affected by the water conductivity.

as pure proton conductors [66]. The lower oxidation state of the aliovalent cation in these materials requires the formation of oxygen vacancies, these results in p-type semiconductor materials whose conductivity in inert flow depends on the movement of the oxygen vacancies.

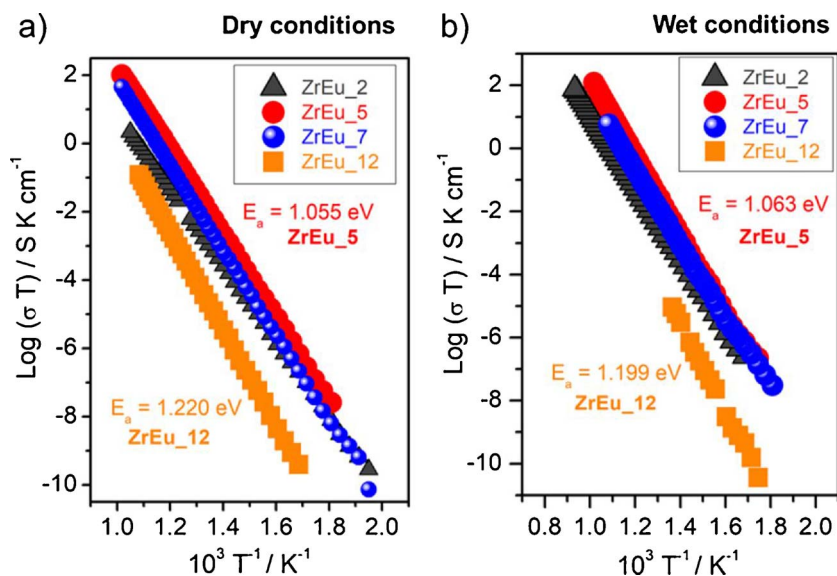


Fig. 8. Conductivity of the samples for all temperature measured range in (a) dry conditions (in Ar atmosphere) and (b) wet conditions with 20% H₂O. Activation energies for the best and the worst samples in both atmospheres calculated by Arrhenius equation.



The impedance behaviour, types of arcs, variation of bulk and grain boundary conductivities as a function of Eu content as well as the increase of the conductivities at higher temperatures is similar to that previously discussed for inert flow for all the analysed atmospheres. The highest total conductivity for the ZrEu_5 sample is the highest among the studied materials whatever the oxygen or water partial pressure used. Moreover, the conductivity is not affected whatever the oxygen partial pressure, data not shown. From 10 to 100 vol.% of oxygen in Ar flow, the impedance responses and the calculated magnitudes are exactly the same for every sample. Thus, the oxygen pressure has not influence on the conduction phenomena. A slight increment of the impedance between 0 and 0.1 oxygen partial pressures is observed; this, probably due to oxygen adsorbed on the conductor surface according to a Langmuir adsorption behaviour. Surface vacancy filling by gaseous phase oxygen should result in a vacancy annihilation and therefore in a slight conductivity decrease. Once the solid is saturated in oxygen (lower than 10 vol.% of O_2), the conductivity is not affected by the oxygen partial pressure. In order to verify this possible oxygen adsorption, other characterization techniques will be necessary.

On the other side, the experiments with different water pressures (represented at 350 °C in Fig. 7b), show that the impedance arcs are modified by the water presence. Consequently, besides the vacancy movement, the conduction behaviour is affected by water presence; this may indicate that the Grotthuss' mechanism operates in these solids in good agreement with Scherrer et al.' work of YSZ compounds [66]. In principle, the conductivity should depend on the concentration of oxygen vacancies, being higher on increasing the number of oxygen vacancies; however, the ZrEu_5 solid shows the highest conductivity in all the tested conditions (inert, oxygen and wet atmospheres). This is explained by some authors as a consequence of the association of oxygen vacancies and dopant ions, thereby blocking the movement of the holes, which results in a decrease of the conductivity [8,67,68]. Both, the increase in the number of oxygen vacancies and the oxygen vacancy-dopant ion association result in a maximum in the conductivity at 5 mol.% europium doping. The activation energy calculation shows an insignificant change of their values as a function of the Eu content increasing proportionally to the europium content, thus supporting the idea of an association of the oxygen vacancies.

Finally, it is important to notice that on increasing temperature the impedance decrease although for the highest temperatures tested the impedance in either Ar or $\text{H}_2\text{O}/\text{Ar}$ (Fig. 9) is hardly different. The differences in the impedance at low temperatures must be related to the presence of adsorbed water on the ionic conductor surface that is

significant at low temperatures and almost negligible at higher temperatures [66]. However, to assess the influence of water in the conductivity, a further characterisation of the adsorbed species on $\text{H}_2\text{O}/\text{Ar}$ atmospheres was performed by *in situ* Raman spectroscopy and DRIFTS measurements.

3.4. *In situ* spectroscopic studies

In order to understand the role of water *in situ* spectroscopic studies were carried out for the highest conductivity sample, ZrEu_5, and, for the sake of comparison, for the sample with the smallest conductivity within the ones tested, ZrEu_12.

In situ Raman studies were carried out in $\text{H}_2\text{O}/\text{N}_2$ flow from 200 °C to 450 °C with a previous activation in N_2 flow at 450 °C for 1 h to dehydrate the sample. The spectra for both samples in wet conditions as a function of temperature are shown in Fig. 10 together with the spectra of the activated samples. The number, positions and relative intensities of all the bands are similar for both N_2 and $\text{H}_2\text{O}/\text{N}_2$ atmospheres whatever the temperature tested. It is evident that both samples exhibit the same profile than *ex situ* Raman spectra performed at room temperature (see Fig. 6). In order to compare the activation step and the experiments with $\text{H}_2\text{O}/\text{N}_2$ flow, it has been displayed the last spectrum at 450 °C in N_2 with the spectra in $\text{H}_2\text{O}/\text{N}_2$ in temperature for each sample. Comparing the profiles at 450 °C in dry and wet conditions, it can be noticed that the intensity and the Raman shift positions hardly changes. The intensity ratio $(\text{F}_2 \rightarrow \text{D}_0)/(\text{F}_1 \rightarrow \text{D}_0)$ increases less than 5% upon heating 450 °C, this must be related to the homogeneous distribution of the europium within solid solution which results just in the modification of the europium sites at the surface upon dehydration.

In situ DRIFTS measurements were used to describe the effect of physisorbed and/or dissociated water in the ionic conductivity. Firstly, the samples were pretreated at 600 °C for 1 h under flow of H_2/Ar to dehydrate the sample and eliminate the water adsorbed on the surface. The initial spectra and the final spectra after the pretreatment are shown in Fig. 11a and b, respectively. As can be observed in Fig. 11a, both ZrEu_5 and ZrEu_12 samples before activation are highly hydrated and the spectra are dominated by a very broad absorption band centered at 3300 cm^{-1} that can be assigned to the OH stretching modes of both undissociated water molecules and hydroxyl species interacting by hydrogen-bonding [69]. On the counterpart, the bending mode associated to the vibration δ_{HOH} appears as a shoulder at 1647 cm^{-1} that can be attributed to non-dissociated/physisorbed water and also contains contributions from lone-pair Lewis-coordinated water [69,70]. The intensities of these bands in both samples suggest a lower ability to absorb water of the ZrEu_12 sample. On the other hand, the set of

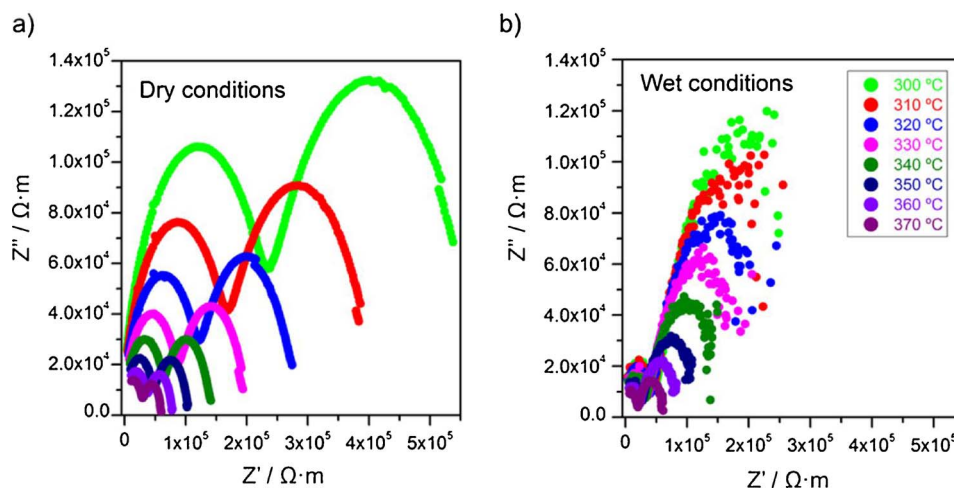


Fig. 9. Complex plane plots of the impedance spectroscopy of the sintered samples at different temperatures in (a) dry conditions (in Ar atmosphere) and (b) wet conditions with 20% H_2O .

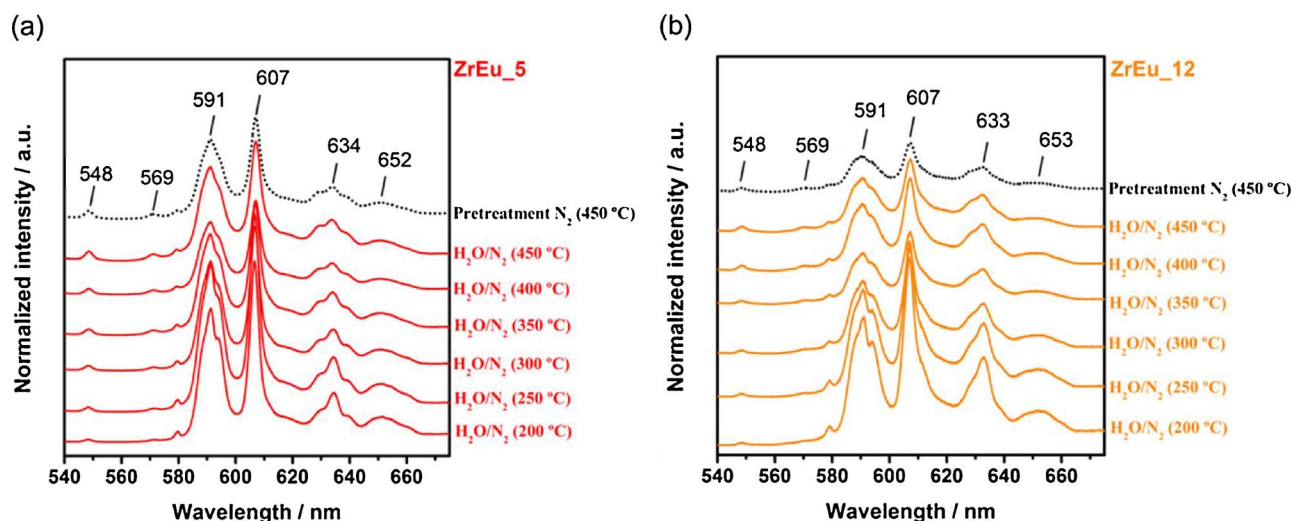


Fig. 10. Luminescence spectra extracted from *in situ* Raman spectroscopy of the samples ZrEu_5 (a) and ZrEu_12 (b) in wet conditions from 200 °C to 450 °C and in dry conditions at 450 °C for comparison.

features that appear in the $1100\text{--}1600\text{ cm}^{-1}$ range in both samples can be assigned to residual carbonates/carboxylates like compounds [70]. The presence of these species is unavoidable since the atmospheric CO_2 adsorption on zirconia and Eu-doped zirconia leads to the formation of carbonate species during the calcination process remaining occluded in the structure of pores of these materials. As revealed by high resolution electron microscopy (HREM), the samples present a significant amount of micropores with size ranging from 2 to 3 nm and carbonate species can be anchored in these cavities. This observation is in good agreement with the results reported by Daturi et al. [71]. The spectral dehydration pattern of both ZrEu_5 and ZrEu_12 samples are presented in Fig. 11b. After treatment at 600 °C in flow of H_2/Ar , it is noticeable the disappearance of the broad band associated to non-dissociated water in the ZrEu_5 sample and the appearance of a new hydroxyl species. The interaction *via* hydrogen-bonds between the water molecules and the hydroxyl species is responsible for the non-appearance of this hydroxyl bands before activation. Additionally, it can be observed a new band around 2100 cm^{-1} that has been attributed to CO occluded in the pores or cavities as will be discussed later. In contrast, the sample ZrEu_12

presents the broad band around 3300 cm^{-1} observed before activation (decreased in intensity) and any new band attributable to OH species is detected.

We investigate now the effect of water adsorption in the 200–450 °C temperature range on the surface of ZrEu_5 and ZrEu_12 samples after activation. These results are presented in two different wavenumber regions: $3800\text{--}3200\text{ cm}^{-1}$ for hydroxyl groups and $3000\text{--}2000\text{ cm}^{-1}$ for the ${}^7\text{F}_0 \rightarrow {}^7\text{F}_J$ electronic transitions of Eu and possible CO occluded in the pores. As can be noted in the wavenumber region for OH-stretching modes, the activated sample ZrEu_5 (Fig. 12a) clearly shows two new bands at 3765 and 3675 cm^{-1} , respectively, ascribable to the ν_{OH} stretching modes of terminal and tribridged hydroxyl groups [69], that are formed during the activation by water desorption. Under a flow of $\text{H}_2\text{O}/\text{Ar}$, the appearance of a broad band centered at around 3720 cm^{-1} suggests the formation of a “new” type of hydroxyls. A more detailed analysis of difference spectra (taking as reference the spectrum of the activated surface) clearly evidences the decrease of the bands at 3765 and 3675 cm^{-1} and that the broad feature observed at 3720 cm^{-1} is composed by two bands 3700 and 3724 cm^{-1} (Fig. 13). According to

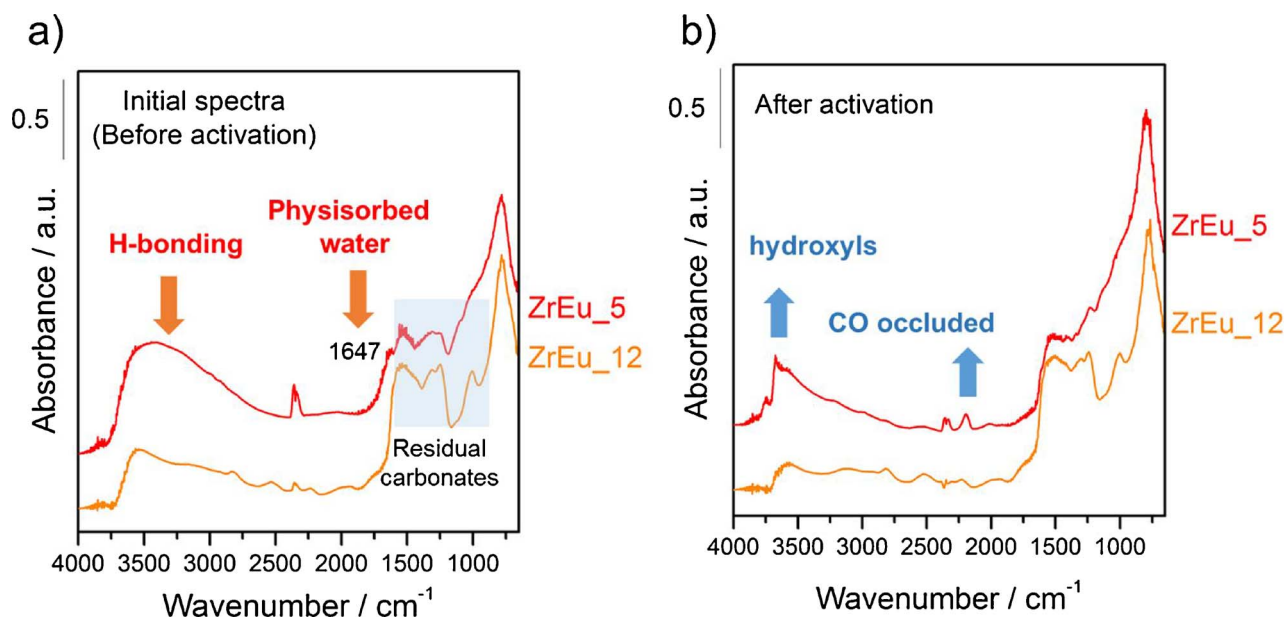


Fig. 11. *In situ* DRIFTS measurement at room temperature before activation (a) and at 200 °C after activation (b) for the samples ZrEu_5 and ZrEu_12.

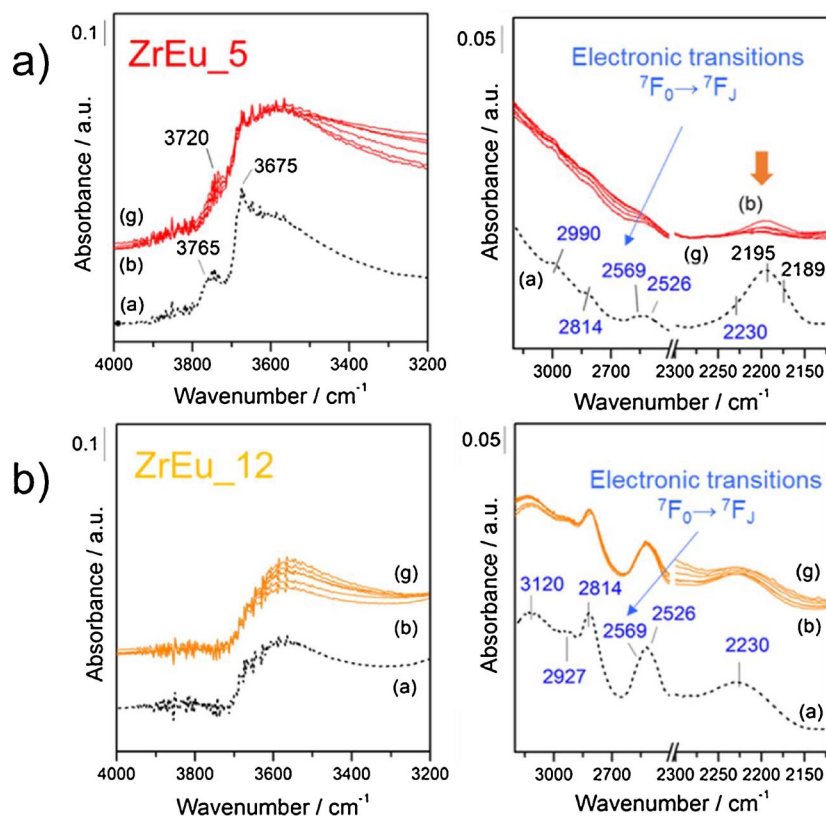


Fig. 12. DRIFTS difference spectra in wet conditions respect to the dried spectrum after activation step (spectra a), from 200 °C (spectra b) to 450 °C (spectra g).

Cerrato et al. [69], hydroxyls type (I) of monoclinic ZrO_2 interacts weakly with water molecules, which provokes a shift to lower wavenumbers (from 3775 cm^{-1} to 3695 cm^{-1}). These data permit us attribute the band at 3700 cm^{-1} to type (I) hydroxyls weakly interacting with water molecules. However, the interaction of hydroxyls at 3675 cm^{-1} (tribridged, more acidic ones) with water is stronger and generates a broad band at lower wavenumbers (3300 cm^{-1}). The “new” band appearing in presence of water at 3724 cm^{-1} , may be tentatively attributed to hydroxyls type (II) [69]. Most authors stand up for the absence of these hydroxyls in monoclinic ZrO_2 due to the short Zr-Zr distance ($\sim 2\text{ \AA}$) in this structure that impedes the stabilization of OH bonded to two metallic cations. In the case of stabilized cubic zirconia doped with trivalent cations, the metal-metal distance become larger [72] and the presence of OH(II) may be possible. Therefore, we propose that this band is associated to the presence of oxygen vacancies created

by doping with Eu^{3+} .

As the temperature increases (from 200 °C to 400 °C) the band at 5248 cm^{-1} corresponding to $(\nu + \delta(\text{HOH}))$ combination bands of water molecules [73] progressively decreases, being completely absent when the temperature reaches 300 °C. In these conditions, the band at 3724 cm^{-1} is still observed at the same position, which suggests that these hydroxyls groups do not interact with the water molecules. We believe that the -OH generation takes place on the vacancies on every structural defect close to the Eu centers. This explanation is in good agreement with Köck et al. [74]. They found that the doping of zirconia with Y_2O_3 creates defects near the Y^{3+} centers in which new hydroxyls groups can be formed. From these observations, we may propose a surface on which free OH groups and water molecules coexist, providing an adequate situation to favours the Grotthuss’ mechanism at least at temperatures lower than 300 °C [75].

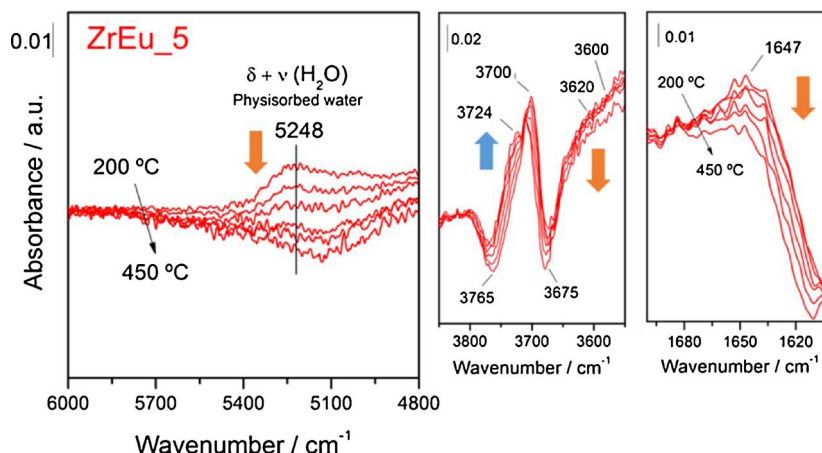


Fig. 13. DRIFTS difference spectra of ZrEu₅ sample in wet conditions respect to the dried spectrum after activation step from 200 °C to 450 °C magnifying water adsorption regions.

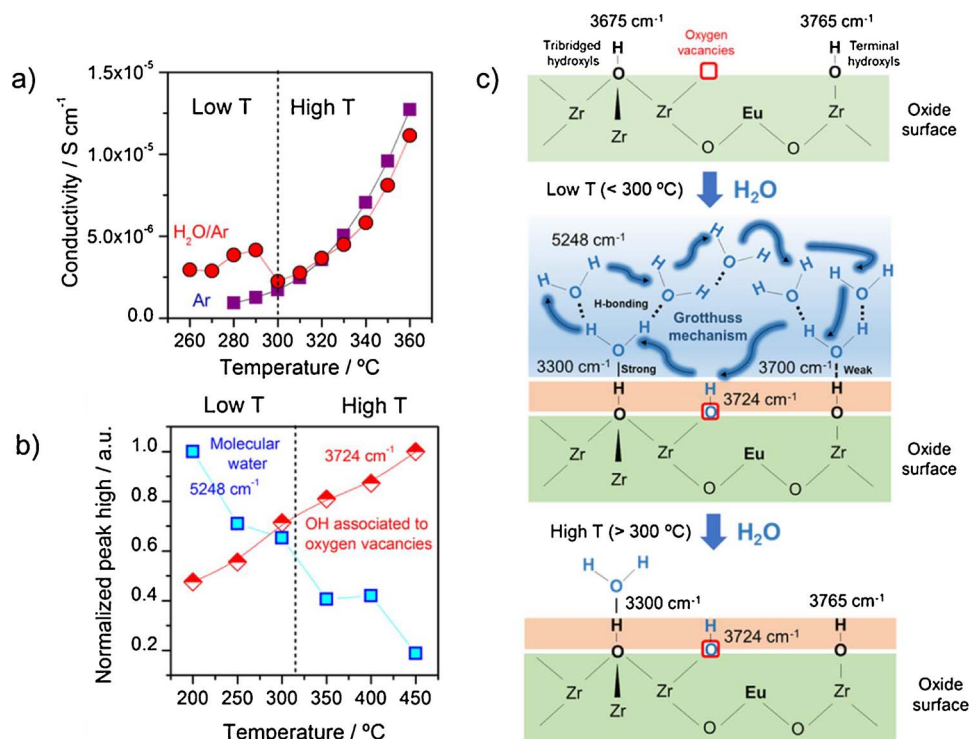


Fig. 14. (a) Ionic conductivity of the sample ZrEu₅ in dry (Ar) and wet conditions. (b) Variation of the normalized intensity with the temperature of the bands associated to physisorbed water (5248 cm⁻¹) and dissociated water (3724 cm⁻¹) of sample ZrEu₅ analysed by DRIFTS in wet conditions. (c) Water layer model proposed for the Eu doped ZrO₂ samples and the effect of the water and the temperature.

In the 3000–2000 cm⁻¹ region, it is evident the presence of different bands that corresponding to low energy transitions from the ⁷F ground term to the ⁷F_J levels. This type of transitions are characteristic of Eu³⁺ ions doped inorganic matrices and can be observed by Infrared spectroscopy due to its low energy [57]. Additionally, after activation a feature composed by two bands at 2195 and 2189 cm⁻¹ that are characteristic of CO confined in the cavities of the material pores is observed [71]. The occluded carbonates in the pores of the material are reduced in presence of hydrogen generating CO that remains anchored inside the cavities. The treatment with water upon increasing temperature leads to the complete disappearance of both ν(CO) bands forming likely again carbonate species that are reversibly restored with the treatment. According to the model proposed by Daturi et al. [71], the treatment under hydrogen at 600 °C produces a confined reduction of the surface mobilizing oxygens from the bulk and changing partially the coordination inside the cavities. The reoxidation with water produces a reconstitution of the previous carbonate species inside the cavities or additionally generate new hydroxyl species by dissociation of water at the oxygen vacancies.

Fig. 12b shows the effect of the adsorption of water as a function of temperature after activation for the sample ZrEu₁₂. We must notice that this sample present a completely different behaviour to that of the ZrEu₅ sample and the presence of free hydroxyls after activation is much lower. In consequence, the amount of adsorbed water could be negligible since the number of centers available for interaction via H–bond is restricted. As it is well-known, ionic conductivity of pure zirconia is improved by the introduction of acceptor dopants like Eu that besides stabilize the cubic structure at low temperatures and increase the concentration of oxygen vacancies [8]. However, a large amount of dopant element can result prejudicial and the improvement of ionic conductivity is no longer observed as it has been analysed above. Moreover, the possible formation of segregated europia phases in the ZrEu₁₂ sample as well as the lower specific surface, may result in a decrease in the presence of hydroxyls on the surface and thereby the interaction with the water molecules. In the 3000–2000 cm⁻¹ wavenumber region, the intensity of the bands associated to the f–f electronic transitions are notably increased due to the higher concentration of europium. However, the bands associated to the CO occluded do not

appear. This fact can be explained considering that the concentration of pores in this sample is significantly lower as can be observed by TEM (Fig. 3).

Raz et al. [76] investigated the adsorption of water layers on yttrium stabilized zirconia and suggested the first water layer to be chemisorbed on the Zr sites whereas the second layer is physisorbed on top of the chemisorbed water layer. We propose an analogous model in which the dissociation of water takes place on the vacancies. Thus, the dissociation of water molecules takes place on specific sites generating hydroxyl species whereas the coordination of undissociated water occurs through interactions with the surface hydroxyls.

As we mentioned above, the enhancement of the conductivity caused by the inclusion of the water is distinguishable at low temperature but is negligible at high temperature (from 300 °C) as it is shown by its impedance response in Fig. 9 or by its conductivity data in Fig. 14a. This behaviour can be explained by desorption of the water because of the temperature increase, hence it is obtained the same value of conductivity as in argon atmosphere for high temperature. Moreover, the band at 5248 cm⁻¹ ascribed above to the physisorbed water, also disappears for high temperature (Fig. 13). Concretely, in Fig. 14b, it can be noted that the intensity of the physisorbed water band decreases with temperature and above 300 °C the signal is almost zero. Though the band associated to hydroxyl groups generated on the surface vacancies (3724 cm⁻¹) is increasing as we can see in Fig. 14b, we can conclude that the ionic conduction phenomena are influenced and improved by the presence of physisorbed water available for the Grotthuss' mechanism according to the impedance and DRIFTS analysis as well as Scherrer et al.' work [66]. Therefore, the conductivity of these europium doped zirconia samples is the same in both inert and wet conditions at high temperature (from 300 °C) due to the absence of physisorbed water from this temperature. At lower temperatures, on the other side, the dissociated water in the oxygen vacancies (band at 3730 cm⁻¹) and the adsorbed water create layers of water molecules whose interaction allows proton conductivity by Grotthuss' mechanism increases the total conductivity in this temperature range. This layer model represented in Fig. 14c is in agreement with the model suggested by Kock et al. [74].

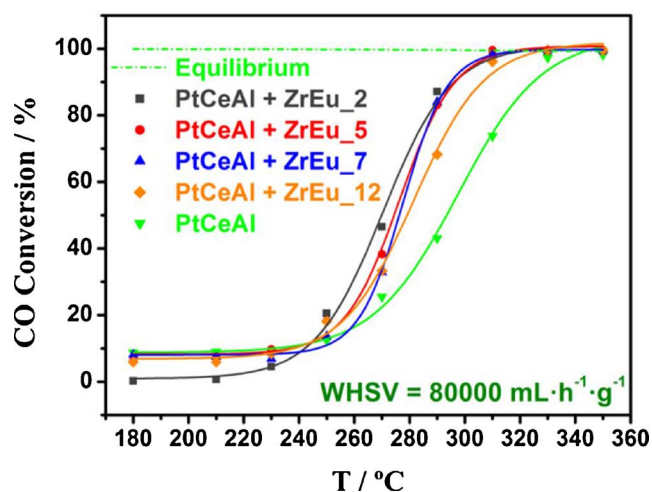


Fig. 15. Catalytic tests in WGS reaction on PtCeAl + ZrEu_x (1:5) compared to the activity of the bare PtCeAl catalyst.

3.5. Catalytic tests in WGS reaction on proton conductor-promoted PtCeAl catalyst

The WGS reaction has been carried out in the conditions mentioned above. The activity exhibited by the bare PtCeAl sample (Fig. 15) is in agreement with other Pt based catalysts found elsewhere [77,78]. In this work has been used a high space velocity in order to avoid getting the maximum conversion easily to see the influence of the ionic conductor. Thus, the effect of these promoted catalysts should be noticeable. Moreover, according to a future applicability in mobile devices [79], the favourable effect of a proton conductor is indeed interesting at high space velocity.

The activities of the promoted catalyst (physical mixtures of catalyst and proton conductor) displayed in terms of CO conversion show that the presence of the conducting material enhances the performance of the catalyst with all ZrEu series. In addition, it is noticeable that the increment of CO conversion with physical mixtures catalysts appears at 270–290 °C, where the catalyst operates by itself. Thus, this improvement is according to an effect of the proton conductor. This may be related to the assistance to the catalyst in the water activation step, since the promotion only is observed when the catalyst presents activity. Not surprisingly, the presence of proton conductor materials provides the PtCeAl catalyst more available dissociated water improving the performance of the water activation. Thus, the catalytic systems that include proton conductors exhibit more activity in WGS reaction but only in the temperature range that the bare PtCeAl catalyst operates, since the ionic conductor only acts as water-enhancer at the service of the catalyst. Moreover, the differences in the activity plots showed in Fig. 15 only depend on the features of the proton conductors. In fact, it is highlighted the lower effect for ZrEu₁₂ sample than for the rest physical mixtures. The ZrEu₁₂ sample provides the water activation effect since it is a proton conductor; however, according to the results of the conductivity analysis by impedance spectroscopy, this sample exhibits meaningful lower conductivity and higher activation energy than the rest (ZrEu₂, ZrEu₅ and ZrEu₇ samples). Therefore, the significantly lower activity of the PtCeAl + ZrEu₁₂ system than the rest physical mixtures is expected. On the other side, the ZrEu₂, ZrEu₅ and ZrEu₇ samples show similar conductivity values and higher than ZrEu₁₂ sample, especially at operation temperature range of WGS reaction. This fact is also reflected in the catalytic tests, where the systems formed by PtCeAl catalyst and these proton conductors provide the highest CO conversion plots.

According to the previously exposed, the ionic conductor increases the activity of the catalyst in terms of CO conversion due to its capacity to dissociate water and develop Grotthuss' conductivity. The proton

conductor helps the water activation. Moreover, in agreement with these observations, ionic conductors and diluent quartz were tested in WGS reaction in the same conditions without catalyst in contemplation of verifying their catalytic inactivity. These results support again the role of the proton conductors as water-enhancer species but not as active catalysts by themselves.

In this sense, as it was mentioned in the introduction section, it has been studied by our research group the ionic conductor effect with different WGS catalysts which operate by different mechanisms [45]. That work revealed again an evident promoter effect in the temperature range in which the activity of the catalyst starts to be appreciable. Therefore, the catalyst or the ionic conductor, the latter helps the water activation according to the proper mechanism of the catalyst.

4. Conclusions

A series of europium doped zirconia compounds (2–15 mol.% of Eu₂O₃) has been synthesized by precipitation. Fluorite-type cubic solid solutions are produced for dopant contents up to 9 mol.% and segregated Eu oxide appearing for higher contents. The samples show a decrease of the S_{BET} and the porous volume when the quantity of the Eu dopant increases, but all of them exhibit homogeneous distribution of the dopant and, consequently, of the oxygen vacancies, and porosity with monomodal distribution between 2 and 3 nm. Representative samples (ZrEu₂, ZrEu₅, ZrEu₇ and ZrEu₁₂) were also analysed by impedance spectroscopy in inert, oxygen and wet conditions. The experiments show the increment of the conductivity with the temperature typical of a p-type semiconductor created by the presence of oxygen vacancies exhibiting activation energies around 1 eV according to a pure ionic conductor. Moreover, the comparative between the different samples reveals a maximum conductivity for the ZrEu₅ sample in every tested condition in agreement with others studies where the ionic conductivity requires the presence of the oxygen vacancies but an increment of the dopant content implies lower conductivity due to the association between the oxygen vacancies and the dopant ions.

The impedance spectroscopy also shows that the conductivity is affected by water. Certainly, wet conditions increase the conductivity at low temperature (until ~300 °C). Temperatures higher than 300 °C exhibit the same conductivity than in inert atmosphere, thereby being negligible the water contribution from this temperature. According to DRIFTS and impedance analysis, we conclude a layer model where the dissociated water in the oxygen vacancies interacts with adsorbed water improving the conductivity by Grotthuss' mechanism. When the temperature exceeds 300 °C, the physisorbed water disappears because of the high temperature and exhibiting the same conductivity than in inert conditions.

These experiments reveal that the synthesized europium doped zirconia compounds are pure proton conductors whose conductivity is improved at low temperatures in wet conditions. Therefore, in agreement with was exposed above, the addition of these kind of ionic conductors in a catalytic system where the diffusion of the water was a rate-limiting step like WGS reaction, can play an important role in its performances. Thus, the catalytic tests show better catalyst' activity in terms of CO conversion when it is mixed with these proton conductors. Moreover, the improvement appears when the catalyst starts to work indicating that the Eu-doped ZrO₂ proton conductors act as a water-enhancer for the water-activation limiting step.

Acknowledgement

Financial support for this work was obtained from the Spanish Ministerio de Economía y Competitividad (MINECO) (ENE2015-66975-C3-2-R).

References

- [1] V. Nalini, R. Haugsrud, T. Norby, High-temperature proton conductivity and defect structure of TiP_2O_7 , *Solid State Ionics* 181 (2010) 510–516.
- [2] K.R. Kendall, C. Navas, J.K. Thomas, H.-C. zur Loye, Recent developments in oxide ion conductors: aurivillius phases, *Chem. Mater.* 8 (1996) 642–649.
- [3] Z. Gao, L.V. Mogni, E.C. Miller, J.G. Railsback, S.A. Barnett, A perspective on low-temperature solid oxide fuel cells, *Energy Environ. Sci.* 9 (2016) 1602–1644.
- [4] M. Huse, T. Norby, R. Haugsrud, Effects of A and B site acceptor doping on hydration and proton mobility of LaNbO_4 , *Int. J. Hydrog. Energy* 37 (2012) 8004–8016.
- [5] S. Stølen, E. Bakken, C.E. Mohn, Oxygen-deficient perovskites: linking structure, energetics and ion transport, *Phys. Chem. Chem. Phys.* 8 (2006) 429–447.
- [6] R.J.D. Tilley, *Defects in Solids*, WILEY, New Jersey, 2008.
- [7] J. Sunarso, S. Baumann, J.M. Serra, W.A. Meulenbergh, S. Liu, Y.S. Lin, J.C. Diniz, da Costa, Mixed ionic-electronic conducting (MIEC) ceramic-based membranes for oxygen separation, *J. Membr. Sci.* 320 (2008) 13–41.
- [8] L. Malavasi, C.A.J. Fisher, M.S. Islam, Oxide-ion and proton conducting electrolyte materials for clean energy applications: structural and mechanistic features, *Chem. Soc. Rev.* 39 (2010) 4370–4387.
- [9] K.-D. Kreuer, Proton conductivity: materials and applications, *Chem. Mater.* 8 (1996) 610–641.
- [10] S. Wang, Y. Chen, S. Fang, L. Zhang, M. Tang, K. An, K.S. Brinkman, F. Chen, Novel chemically stable $\text{Ba}_2\text{Ca}_{11}\text{Nb}_{1.82-x}\text{Y}_x\text{O}_{9-8}$ proton conductor: improved proton conductivity through tailored cation ordering, *Chem. Mater.* 26 (2014) 2021–2029.
- [11] K.D. Kreuer, Aspects of the formation and mobility of protonic charge carriers and the stability of perovskite-type oxides, *Solid State Ionics* 125 (1999) 285–302.
- [12] P. Thangadurai, V. Sabarinathan, A.C. Bose, S. Ramasamy, Conductivity behaviour of a cubic/tetragonal phase stabilized nanocrystalline La_2O_3 -ZrO₂, *J. Phys. Chem. Solids* 65 (2004) 1905–1912.
- [13] B. Meredig, C. Wolverton, Dissolving the periodic table in cubic zirconia: data mining to discover chemical trends, *Chem. Mater.* 26 (2014) 1985–1991.
- [14] A. Magrasó, C. Kjølsøth, R. Haugsrud, T. Norby, Influence of Pr substitution on defects, transport, and grain boundary properties of acceptor-doped BaZrO_3 , *Int. J. Hydrog. Energy* 37 (2012) 7962–7969.
- [15] P. Babilo, T. Uda, S.M. Haile, Processing of yttrium-doped barium zirconate for high proton conductivity, *J. Mater. Res.* 22 (2007) 1322–1330.
- [16] J.A. Labrincha, J.R. Prade, F.M.B. Marques, Protonic conduction in $\text{La}_2\text{Zr}_2\text{O}_7$ -based pyrochlore materials, *Solid State Ionics* 99 (1997) 33–40.
- [17] V. Besikiotis, S. Ricote, M.H. Jensen, T. Norby, R. Haugsrud, Conductivity and hydration trends in disordered fluorite and pyrochlore oxides: a study on lanthanum cerate-zirconate based compounds, *Solid State Ionics* 229 (2012) 26–32.
- [18] X.-L. Xia, Z.-G. Liu, J.-H. Ouyang, Y. Zheng, Preparation, structural characterization, and enhanced electrical conductivity of pyrochlore-type $(\text{Sm}_{1-x}\text{Eu}_x)_2\text{Zr}_2\text{O}_7$ ceramics, *Fuel Cells* 12 (2012) 624–632.
- [19] C.-R. Chang, Z.-Q. Huang, J. Li, The promotional role of water in heterogeneous catalysis: mechanism insights from computational modeling, *Wiley Interdiscip. Rev. Comput. Mol. Sci.* 6 (2016) 679–693.
- [20] J.P. Clay, J.P. Greeley, F.H. Ribeiro, W.N. Delgass, W.F. Schneider, DFT comparison of intrinsic WGS kinetics over Pd and Pt, *J. Catal.* 320 (2014) 106–117.
- [21] A.A. Phatak, N. Koryabkina, S. Rai, J.L. Ratts, W. Ruettinger, R.J. Farrauto, G.E. Blau, W.N. Delgass, F.H. Ribeiro, Kinetics of the water-gas shift reaction on Pt catalysts supported on alumina and ceria, *Catal. Today* 123 (2007) 224–234.
- [22] B. Smith R.J., M. Loganathan, M. Shekhar Shantha, A review of the water gas shift reaction kinetics, *Int. J. Chem. Reactor Eng.* 8 (2010) 1–32.
- [23] A.A. Phatak, W.N. Delgass, F.H. Ribeiro, W.F. Schneider, Density functional theory comparison of water dissociation steps on Cu, Au, Ni, Pd, and Pt, *J. Phys. Chem. C* 113 (2009) 7269–7276.
- [24] M. González-Castaño, S. Ivanova, O.H. Laguna, L.M. Martínez T, M.A. Centeno, J.A. Odriozola, Structuring $\text{Pt/CeO}_2/\text{Al}_2\text{O}_3$ WGS catalyst: introduction of buffer layer, *Appl. Catal. B Environ.* 200 (2017) 420–427.
- [25] C.M. Kalamaras, D.D. Dionysiou, A.M. Efstathiou, Mechanistic studies of the water-gas shift reaction over $\text{Pt/Ce}_x\text{Zr}_{1-x}\text{O}_2$ catalysts: the effect of Pt particle size and Zr dopant, *ACS Catal.* 2 (2012) 2729–2742.
- [26] A. Michaelides, P. Hu, Catalytic water formation on platinum: a first-principles study, *J. Am. Chem. Soc.* 123 (2001) 4235–4242.
- [27] L.C. Grabow, A.A. Gokhale, S.T. Evans, J.A. Dumesic, M. Mavrikakis, Mechanism of the water gas shift reaction on Pt: first principles, experiments, and microkinetic modeling, *J. Phys. Chem. C* 112 (2008) 4608–4617.
- [28] D.C. Grenoble, M.M. Estadt, D.F. Ollis, The chemistry and catalysis of the water gas shift reaction, *J. Catal.* 67 (1981) 90–102.
- [29] G. Germani, P. Alphonse, M. Courtney, Y. Schuurman, C. Mirodatos, Platinum/ceria/alumina catalysts on microstructures for carbon monoxide conversion, *Catal. Today* 110 (2005) 114–120.
- [30] X. Liu, O. Korotkikh, R. Farrauto, Selective catalytic oxidation of CO in H_2 : structural study of Fe oxide-promoted Pt/alumina catalyst, *Appl. Catal. A Gen.* 226 (2002) 293–303.
- [31] L. Grabow, Y. Xu, M. Mavrikakis, Lattice strain effects on CO oxidation on Pt(111), *Phys. Chem. Chem. Phys.* 8 (2006) 3369–3374.
- [32] P. Thormählen, M. Skoglundh, E. Fridell, B. Andersson, Low-temperature CO oxidation over platinum and cobalt oxide catalysts, *J. Catal.* 188 (1999) 300–310.
- [33] S.C. Ammal, A. Heyden, Water-gas shift catalysis at corner atoms of Pt clusters in contact with a TiO_2 (110) support surface, *ACS Catal.* 4 (2014) 3654–3662.
- [34] D.R. Mullins, The surface chemistry of cerium oxide, *Surf. Sci. Rep.* 70 (2015) 42–85.
- [35] Y.-G. Wang, D. Mei, J. Li, R. Rousseau, DFT + U study on the localized electronic states and their potential role during H_2O dissociation and CO oxidation processes on CeO_2 (111) surface, *J. Phys. Chem. C* 117 (2013) 23082–23089.
- [36] C.J. Guild, D. Vovchok, D.A. Kriz, A. Bruix, B. Hammer, J. Llorca, W. Xu, A. El-Sawy, S. Biswas, J.A. Rodriguez, S.D. Senanayake, S.L. Suib, S.D. Senanayake, S.L. Suib, Water-gas-shift over metal-free nanocrystalline ceria: an experimental and theoretical study, *ChemCatChem* 9 (2017) 1373–1377.
- [37] L. Gill, A. Beste, B. Chen, M. Li, A.K.P. Mann, S.H. Overbury, E.W. Hagaman, Fast MAS ^1H NMR study of water adsorption and dissociation on the (100) surface of ceria nanocubes: a fully hydroxylated, hydrophobic ceria surface, *J. Phys. Chem. C* 121 (2017) 7450–7465.
- [38] Y. Lykhach, V. Johánek, H.A. Aleksandrov, S.M. Kozlov, M. Happel, T. Skála, P.St. Petkov, N. Tsud, G.N. Vayssilov, K.C. Prince, K.M. Neyman, V. Matolin, J. Libuda, Water chemistry on model ceria and Pt/ceria catalysts, *J. Phys. Chem. C* 116 (2012) 12103–12113.
- [39] C.M. Kalamaras, K.C. Petalidou, A.M. Efstathiou, The effect of La^{3+} -doping of CeO_2 support on the water-gas shift reaction mechanism and kinetics over $\text{Pt/Ce}_{1-x}\text{La}_x\text{O}_2$, *Appl. Catal. B Environ.* 136–137 (2013) 225–238.
- [40] G. Jacobs, U.M. Graham, E. Chenu, P.M. Patterson, A. Dozier, B.H. Davis, Low-temperature water-gas shift: impact of Pt promoter loading on the partial reduction of ceria and consequences for catalyst design, *J. Catal.* 229 (2005) 499–512.
- [41] T. Ramírez Reina, W. Xu, S. Ivanova, M.A. Centeno, J. Hanson, J.A. Rodriguez, J.A. Odriozola, In situ characterization of iron-promoted ceria-alumina gold catalysts during the water-gas shift reaction, *Catal. Today* 205 (2013) 41–48.
- [42] A. Trovarelli, Catalytic properties of ceria and CeO_2 -containing materials, *Catal. Rev.* 38 (1996) 439–520.
- [43] J.A. Rodriguez, J.C. Hanson, D. Stacchiola, S.D. Senanayake, In situ/operando studies for the production of hydrogen through the water-gas shift on metal oxide catalysts, *Phys. Chem. Chem. Phys.* 15 (2013) 12004–12025.
- [44] S. Aranifard, S.C. Ammal, A. Heyden, On the importance of the associative carboxyl mechanism for the water-gas shift reaction at Pt/ CeO_2 interface sites, *J. Phys. Chem. C* 118 (2014) 6314–6323.
- [45] J.A. Odriozola, S. Ivanova, F. Romero-Sarria, N. García-Moncada, M. González-Castaño, M.A. Centeno, (2017), Spanish Patent ES 2 595 937 A1 “Complejo catalítico conformado por la mezcla de catalizador y conductor iónico,”.
- [46] Y.K. Voronko, M.A. Zafarov, A.A. Zabol, L.I. Taymbal, Site-selective spectroscopy and nearest neighbor environment of Eu^{3+} in monoclinic $\text{ZrO}_2\text{-Ln}_2\text{O}_3$ and $\text{HfO}_2\text{-Ln}_2\text{O}_3$ solid solutions, *Inorg. Mater.* 32 (1996) 1063–1068.
- [47] P.S. Maram, S.V. Ushakov, R.J.K. Weber, C.J. Benmore, A. Navrotsky, In situ diffraction from levitated solids under extreme conditions-structure and thermal expansion in the $\text{Eu}_2\text{O}_3\text{-ZrO}_2$ system, *J. Am. Ceram. Soc.* 98 (2015) 1292–1299.
- [48] A. Nakamura, New defect-crystal-chemical approach to non-vegardianity and complex defect structure of fluorite-based $\text{MO}_2\text{-Ln}_{0.5}$ solid solutions ($\text{M}^{4+} = \text{Ce}, \text{Th}; \text{Ln}^{3+} = \text{lanthanide}$) part I: model description and lattice-parameter data analysis, *Solid State Ionics* 181 (2010) 1543–1564.
- [49] O. Fabriciynaya, M.J. Krieger, D. Pavlyuchkov, J. Seidel, A. Dzuban, G. Savinykh, G. Schreiber, Heat capacity for the $\text{Eu}_2\text{Zr}_2\text{O}_7$ and phase relations in the $\text{ZrO}_2\text{-Eu}_2\text{O}_3$ system: experimental studies and calculations, *Thermochim. Acta* 558 (2013) 74–82.
- [50] A. Bueno-López, K. Krishna, M. Makkee, J.A. Moulijn, Enhanced soot oxidation by lattice oxygen via La^{3+} -doped CeO_2 , *J. Catal.* 230 (2005) 237–248.
- [51] W.Y. Hernández, M.A. Centeno, F. Romero-Sarria, J.A. Odriozola, Synthesis and characterization of $\text{Ce}_{1-x}\text{Eu}_x\text{O}_{2-x/2}$ mixed oxides and their catalytic activities for CO oxidation, *J. Phys. Chem. C* 113 (2009) 5629–5635.
- [52] S.-Z. Ma, F.-H. Liao, S.-X. Li, M.-Y. Xu, J.-R. Li, S.-H. Zhang, S.-M. Chen, R.-L. Huang, S. Gao, Effect of microstructure, grain size, and rare earth doping on the electrochemical performance of nanosized particle materials, *J. Mater. Chem.* 13 (2003) 3096–3102.
- [53] N. Serpone, Is the band gap of pristine TiO_2 narrowed by anion- and cation-doping of titanium dioxide in second-generation photocatalysts? *J. Phys. Chem. B* 110 (2006) 24287–24293.
- [54] H. Tang, Y. Liu, W. Luo, R. Li, X. Chen, Optical spectroscopy of Eu^{3+} ions in tetragonal ZrO_2 nanocrystals, *J. Nanosci. Nanotechnol.* 11 (2011) 9445–9450.
- [55] J. Yi, Z. Zhao, Y. Wang, D. Zhou, C. Ma, Y. Cao, J. Qiu, Monophasic zircon-type tetragonal $\text{Eu}_{1-x}\text{Bi}_x\text{VO}_4$ solid-solution: synthesis, characterization, and optical properties, *Mater. Res. Bull.* 57 (2014) 306–310.
- [56] J.-G. Kang, Y. Jung, B.-K. Min, Y. Sohn, Full characterization of $\text{Eu}(\text{OH})_3$ and Eu_2O_3 nanorods, *Appl. Surf. Sci.* 314 (2014) 158–165.
- [57] K. Binnemans, Interpretation of europium(III) spectra, *Coord. Chem. Rev.* 295 (2015) 1–45.
- [58] C. Tiseanu, V.I. Parvulescu, B. Cojocaru, K. Pearn, M. Sanchez-Dominguez, M. Boutonnet, In situ Raman and time-resolved luminescence investigation of the local structure of ZrO_2 in the amorphous to crystalline phase transition, *J. Phys. Chem. C* 116 (2012) 16776–16783.
- [59] C. Tiseanu, B. Cojocaru, V.I. Parvulescu, M. Sanchez-Dominguez, P.A. Primus, M. Boutonnet, Order and disorder effects in nano- ZrO_2 investigated by micro-Raman and spectrally and temporally resolved photoluminescence, *Phys. Chem. Chem. Phys.* 14 (2012) 12970–12981.
- [60] P. Ghosh, A. Patra, Role of surface coating in $\text{ZrO}_2/\text{Eu}^{3+}$ nanocrystals, *Langmuir* 22 (2006) 6321–6327.
- [61] M.J. Weber, E.J. Sharp, J.E. Miller, Optical spectra, relaxation, and energy transfer of Eu^{3+} and Cr^{3+} in a europium phosphate glass, *J. Phys. Chem. Solids* 32 (1971) 2275–2284.
- [62] J.P. Goff, W. Hayes, S. Hull, M.T. Hutchings, K.N. Clausen, Defect structure of yttria-stabilized zirconia and its influence on the ionic conductivity at elevated temperatures, *Phys. Rev. B* 59 (1999) 14202–14219.

- [63] S. Karthika, M.S. Sajna, S. Thomas, K.P. Revathy, P.R. Biju, N.V. Unnikrishnan, Structural and optical studies of Eu^{3+} /nanocrystallites doped titania–zirconia hybrids, *J. Alloys Compd.* 615 (2014) 188–193.
- [64] S.M. Haile, D.L. West, J. Campbell, The role of microstructure and processing on the proton conducting properties of gadolinium-doped barium cerate, *J. Mater. Res.* 13 (1998) 1576–1595.
- [65] F.C. Fonseca, R. Muccillo, D.Z. de Florio, L.O. Ladeira, A.S. Ferlauto, Mixed ionic-electronic conductivity in yttria-stabilized zirconia/carbon nanotube composites, *Appl. Phys. Lett.* 91 (2007) 243107–1–243107–3.
- [66] B. Scherrer, M.V.F. Schlupp, D. Stender, J. Martynczuk, J.G. Grolig, H. Ma, P. Kocher, T. Lippert, M. Prestat, L.J. Gauckler, On proton conductivity in porous and dense yttria stabilized zirconia at low temperature, *Adv. Funct. Mater.* 23 (2013) 1957–1964.
- [67] C.-T. Chen, S. Sen, S. Kim, Effective concentration of Mobile oxygen-vacancies in heavily doped cubic zirconia: results from combined electrochemical impedance and NMR spectroscopies, *Chem. Mater.* 24 (2012) 3604–3609.
- [68] A. Navrotsky, Thermodynamics of solid electrolytes and related oxide ceramics based on the fluorite structure, *J. Mater. Chem.* 20 (2010) 10577–10587.
- [69] G. Cerrato, S. Bordiga, S. Barbera, C. Morterra, Surface characterization of monoclinic ZrO_2 . I morphology, FTIR spectral features, and computer modelling, *Appl. Surf. Sci.* 115 (1997) 53–65.
- [70] T. Merle-Méjean, P. Barberis, S. Ben Othmane, F. Nardou, P.E. Quintard, Chemical forms of hydroxyls on/in zirconia: an FT-IR study, *J. Eur. Ceram. Soc.* 18 (1998) 1579–1586.
- [71] M. Daturi, C. Binet, S. Bernal, J.A. Pérez Omil, J.C. Lavalley, FTIR study of defects produced in ZrO_2 samples by thermal treatment. Residual species into cavities and surface defects, *J. Chem. Soc. Faraday Trans.* 94 (1998) 1143–1147.
- [72] P. Li, I.-W. Chen, J.E. Penner-Hahn, Effect of dopants on zirconia stabilization—an X-ray absorption study: I, trivalent dopants, *J. Am. Ceram. Soc.* 77 (1994) 118–128.
- [73] A. Vimont, J.-M. Goupil, J.-C. Lavalley, M. Daturi, S. Surblé, C. Serre, F. Millange, G. Férey, N. Audebrand, Investigation of acid sites in a zeotypic giant pores chromium (III) carboxylate, *J. Am. Chem. Soc.* 128 (2006) 3218–3227.
- [74] E.-M. Köck, M. Kogler, B. Klötzer, M.F. Noisternig, S. Penner, Structural and electrochemical properties of physisorbed and chemisorbed water layers on the ceramic oxides Y_2O_3 , YSZ, and ZrO_2 , *ACS Appl. Mater. Interfaces* 8 (2016) 16428–16443.
- [75] A. Motta, M.-P. Gaigeot, D. Costa, Ab initio molecular dynamics study of the AlOOH boehmite/water interface: role of steps in interfacial grotthus proton transfers, *J. Phys. Chem. C* 116 (2012) 12514–12524.
- [76] S. Raz, K. Sasaki, J. Maier, I. Riess, Characterization of absorbed water layers on Y_2O_3 - doped ZrO_2 , *Solid State Ionics* 143 (2001) 181–204.
- [77] M. Gonzalez Castaño, T.R. Reina, S. Ivanova, M.A. Centeno, J.A. Odriozola, Pt vs. Au in water-gas shift reaction, *J. Catal.* 314 (2014) 1–9.
- [78] N. Dupont, G. Germani, A.C. van Veen, Y. Schuurman, G. Schäfer, C. Mirodatos, Specificities of micro-structured reactors for hydrogen production and purification, *Int. J. Hydrog. Energy* 32 (2007) 1443–1449.
- [79] R.J. Farrauto, Y. Liu, W. Ruettinger, O. Ilinich, L. Shore, T. Giroux, Precious metal catalysts supported on ceramic and metal monolithic structures for the hydrogen economy, *Catal. Rev. Sci. Eng.* 49 (2007) 141–196.